Meshless membrane model based on the moving least-squares method

Hiroshi Noguchi* and Gerhard Gompper†
Institut für Festkörperforschung, Forschungszentrum Jülich, 52425 Jülich, Germany
(Received 25 October 2005; published 10 February 2006; publisher error corrected 14 February 2006)

A meshless particle-based membrane model is proposed. The particles possess no internal degree of freedom and interact via a potential, which has three different contributions: a short-range repulsive pair potential, an attractive multibody potential, and a curvature potential based on the moving least-squares method. Brownian dynamics simulations are employed to demonstrate that the particles self-assemble into a membrane and to study equilibrium properties, such as bending rigidity, surface tension, line tension, and diffusion constant. The bending rigidity and line tension are shown to depend on different potential parameters and can therefore be varied independently. The finite-size effects of nearly planar membranes are investigated. This model is well suited to study the membrane dynamics with topological changes.

DOI: 10.1103/PhysRevE.73.021903 PACS number(s): 87.16.Dg, 87.17.Aa, 82.70.Uv

I. INTRODUCTION

Amphiphilic molecules, like lipids and detergents, form various structures in aqueous solution, such as spherical and cylindrical micelles, and bilayers [1–3]. In particular, bilayer membranes are biologically important as model systems for the plasma membrane and intracellular compartments in living cells. In thermal equilibrium, the shapes of vesicles have been investigated intensively and are now understood very well [3,4]. In comparison, the behavior in nonequilibrium situations is much less explored. Nonequilibrium phenomena are often accompanied by topological changes of membrane. For example, shear flow induces a transition from planar lamellar sheets to multilamellar vesicles [5–8]; in living cells, membrane fusion and fission frequently occur in various processes, such as endo- or exocytosis, protein trafficking, fertilization, and viral infection [3,9,10].

The models of bilayer membranes can be classified into two groups, depending on whether the bilayer structure is implicitly or explicitly taken into account. In the first group, the bilayer membrane is described as a mathematical surface whose shapes and fluctuations are controlled by an elastic energy. This description is valid on length scales much larger than the membrane thickness. The free energy of a fluid membrane is then given by [11]

$$F = \int \left[\gamma + \frac{\kappa}{2}(C_1 + C_2 - C_0)^2 + \bar{\kappa} C_1 C_2 \right] dA, \qquad (1)$$

where C_1 and C_2 are the principal curvatures at each point of the membrane. Here, γ is the surface tension, and κ, $\bar{\kappa}$, and C_0 are the bending rigidity, the saddle-splay modulus, and the spontaneous curvature, respectively. All properties of the molecules forming the bilayer, and their interactions, are only reflected in the values of these elastic parameters. For homogeneous membranes of fixed topology, the integral over the Gaussian curvature $C_1 C_2$ is an invariant, so that their properties are independent of $\bar{\kappa}$. However, the membrane dynamics with topological changes, and the shape near a membrane edge or a boundary between two membrane domains, will, in general, depend on $\bar{\kappa}$ [12,13].

In the second group, the bilayer structure is modeled on an atomic or molecular scale [14–16], and the solvent is taken into account explicitly or implicitly. In coarse-grained models, several atoms are described approximately by one particle or segment [15,16]. The explicit modeling of bilayer structure is necessary, for example, to study the effects of molecular architecture and the pathways of membrane fusion, and the structure and function of membrane proteins in lipid bilayers. However, these models are numerically applicable only for much shorter length and time scales than the curvature models.

In this paper, we focus on the group of curvature elastic models. A discretization of surface is necessary for numerical simulations. The most frequently used approach is to employ triangulated networks [17,18]. The surface is constructed by the positions of surface points (or particles) $\mathbf{r}_i$ and the bond connections (i,j). The distance between points is typically considered to be much larger than the membrane thickness. Thus, one mesh point can correspond to hundreds or thousands of lipid molecules. A triangular mesh has been employed intensively for both solid (or polymerized) [19–21] and fluid [17,18] membranes. In fluid membranes, the triangular mesh is dynamically reconnected by the flipping of bonds by a Monte Carlo (MC) procedure [22–24]. This model has been applied to equilibrium vesicle shapes and fluctuations, as well as to vesicle dynamics in flow [25–27]. In mesh models, a topological change can be taken into account by a discrete procedure with mesh reconnection [18,28]. This has been used to investigate the structure and phase behavior of microemulsions and sponge phases [28].

An alternative, meshless membrane model was proposed by Drouffe *et al.* [29]. The particles possess an orientational degree of freedom and interact with each other via three potentials: a soft-core repulsion, an anisotropic attraction, and a hydrophobic multibody interaction. Particles self-assemble into membrane patches and vesicles. Recently, this model was developed further to describe bilayer membranes [30–37]. These models can be applied naturally to topologi-

*E-mail: hi.noguchi@fz-juelich.de
†E-mail: g.gompper@fz-juelich.de

cal changes. Furthermore, the molecular orientation is important to model a tilt deformation on curved surfaces [38] or bilayer membranes [32,39]. For example, the tilt of the lipids has been suggested to reduce the energy barrier in membrane fusion [40]. Thus, additional degrees of freedom can induce different structures and dynamical behaviors. For the description of phenomena where tilt deformations are not important, a simpler model without internal degrees of freedom is highly desirable because it can be simulated more efficiently.

Our purpose is to construct a membrane model only based on the positions of particles $\mathbf{r}_i$, i.e., without bond connections and intraparticle degrees of freedom. Mesh reconstruction from surface points is a possible candidate. However, the Voronoi reconstruction of nearly touching surfaces is difficult and the results depend on the employed methods [41]. For continuous topological changes, a smoothing procedure similar to smooth Voronoi tessellation in two dimensions [42,43] is required, but a corresponding method for curved surfaces has not been developed thus far.

An alternative approach is the moving least-squares (MLS) method, which is a least-squares fit weighted locally around each particle [32,44–46]. The MLS method has been applied to the discretization of partial differential equations [44], data fitting [45], the rendering of computer graphics [46], and the estimation of normal vectors [32]. We employ the MLS method here to construct a curvature potential of a membrane. We propose two types of potentials. The first potential (model I) is based on a second-order MLS method and explicitly depends on the curvature. However, this model is numerically time consuming and we have performed only a few simulations with this model. The second potential (model II) is based on a first-order MLS method and can be applied to study membrane dynamics accompanied by topological changes. Model II needs much less computational time than model I. In this paper, we focus on the equilibrium properties of the membrane, which are calculated from nearly planar membranes or quasi-spherical vesicles. We simulated the membrane models I and II by a Monte Carlo (MC) and Brownian dynamics (BD) (molecular dynamics with Langevin thermostat) simulations, respectively.

II. MODEL AND METHOD

We consider a system of N particles, which possess no internal degrees of freedom. The particles interact with each other via three potentials: a repulsive soft-core potential U_{rep}, an attractive potential U_{att}, and a curvature potential. All three potentials depend only on the positions $\mathbf{r}_i$ of the particles.

In Secs. II A–II D, the membrane models are introduced. In Sec. II A, we define a cutoff function f_{cut}, which is employed in all interaction potentials. In Sec. II B, we describe two types of curvature potentials, U_{mls2} and U_{α}, which are based on the MLS method. In Sec. II C, we discuss the saddle-splay modulus $\bar{\kappa}$ of the models defined by these curvature potentials. The other interaction potentials, U_{rep} and U_{att}, are introduced in Sec. II D. Particles have an isotropic excluded volume interaction with a diameter σ. U_{att} is a multibody potential. Finally, the simulation methods are explained in Sec. II E.

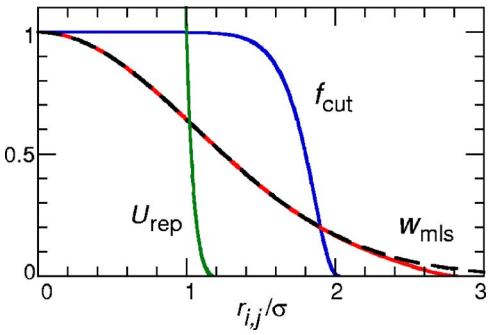

FIG. 1. (Color online) The cutoff function $f_{\mathrm{cut}}(r_{i,j}/\sigma)$ with $n=12$, $s_{\mathrm{half}}=1.8$, and $s_{\mathrm{cut}}=2.1$ [compare Eq. (2)]; the repulsive potential U_{rep}, see Eq. (15); the compact Gaussian weight function $w_{\mathrm{mls}}(r_{i,j})$ with $n=12$ and $r_{\mathrm{cc}}/\sigma=3$, compare Eq. (3). A Gaussian function without cutoff is shown for comparison (dashed line).

A. Cutoff function

A cutoff function is typically employed to reduce computational time in molecular simulations. Most of these functions only possess C^1 or C^2 continuity at the cutoff point. Instead, we propose here the cutoff function

$$f_{\mathrm{cut}}(s)=\begin{cases}\exp\left[A\left(1+\dfrac{1}{(|s|/s_{\mathrm{cut}})^n-1}\right)\right] & (s<s_{\mathrm{cut}})\\ 0 & (s\geqslant s_{\mathrm{cut}})\end{cases}. \quad (2)$$

All orders of derivatives of $f_{\mathrm{cut}}(s)$ are continuous except at $s=0$, where the function is C^{n-1}. This has normally no effect, however, since particles never overlap if they have excluded volume. The parameter A in Eq. (2) is conveniently expressed by the distance s_{half} at which $f_{\mathrm{cut}}(s_{\mathrm{half}})=0.5$, so that $A=\ln(2)\{(s_{\mathrm{cut}}/s_{\mathrm{half}})^n-1\}$. Figure 1 shows an example of $f_{\mathrm{cut}}(s)$. This cutoff function is based on the Stillinger-Webber potential [47], which uses $f_{\mathrm{cut}}(s)$ with $n=1$. With increasing s, the function first decreases slowly from $f_{\mathrm{cut}}(0)=1$ for $s\ll s_{\mathrm{half}}$, then rapidly around $s=s_{\mathrm{half}}$ to $f_{\mathrm{cut}}(s)=0$ for $s\geqslant s_{\mathrm{cut}}$. At larger n, the function decreases more sharply near s_{half}. Thus, the shape of this function can be adjusted easily with the three parameters, n, s_{half}, and s_{cut}.

We employed this function with $n=12$ to cut off the Gaussian and exponential functions. This function can be used as well to cut off other functions, such as Lenard-Jones or Morse potentials.

B. Curvature potential

1. Moving least-squares (MLS) method

Before applying the MLS method to construct curvature potentials, we describe MLS fits of points $\mathbf{r}_i$ on a curved surface in three-dimensional space. We consider MLS fits only at the particle positions $\mathbf{r}_i$ here, but more generally, MLS fits can be calculated at any point in space [46]. A weight function $w_{\mathrm{mls}}(r_{i,j})$ is employed to localize the fitting,

where $r_{i,j}$ is the distance between particles i and j. The weight function is preferentially a compact and monotonic decreasing function of particle distances $r_{i,j}=|\mathbf{r}_i-\mathbf{r}_j|$, with $w_{\mathrm{mls}}(r_{i,j})>0$ inside a subdomain of space, and $w_{\mathrm{mls}}(r_{i,j})=0$ outside. Usually, a spline function is employed for the weight function, but is only C^1 or C^2. Therefore, we propose a Gaussian function modified by the C^∞ cutoff function f_{cut},

$$w_{\mathrm{mls}}(r_{i,j})=\begin{cases}\exp\left(\dfrac{(r_{i,j}/r_{\mathrm{ga}})^2}{(r_{i,j}/r_{\mathrm{cc}})^n-1}\right) & (r_{i,j}<r_{\mathrm{cc}})\\ 0 & (r_{i,j}\geqslant r_{\mathrm{cc}})\end{cases}. \tag{3}$$

This function is smoothly cut off at $r_{i,j}=r_{\mathrm{cc}}$, see Fig. 1. In this paper, we used the parameters $n=12$, $r_{\mathrm{ga}}=0.5r_{\mathrm{cc}}$, and $r_{\mathrm{cc}}=3\sigma$.

In the first-order (linear) MLS method, a plane is fitted to the particle positions by minimizing

$$\Lambda_1(\mathbf{r}_i)=\frac{1}{w_0}\sum_j\{\mathbf{n}\cdot(\mathbf{r}_j-\mathbf{r}_0)\}^2 w_{\mathrm{mls}}(r_{i,j}), \tag{4}$$

where the sum is over all points (including i itself), and $w_0=\Sigma_j w_{\mathrm{mls}}(r_{i,j})$ is a normalization factor. The normal vector $\mathbf{n}$ of the plane and the point $\mathbf{r}_0$ on the plane are fitting parameters. The minimum of Λ_1 is given by $\Lambda_1^{\min}=\lambda_1$ when $\mathbf{r}_0=\mathbf{r}_{\mathrm{G}}\equiv\Sigma_j\mathbf{r}_j w(r_{i,j})/w_0$ is the weighted center of mass and $\mathbf{n}$ is collinear with the eigenvector $\mathbf{u}_1$ of the lowest eigenvalue λ_1 of the weighted gyration tensor

$$a_{\alpha\beta}=\sum_j(\alpha_j-\alpha_{\mathrm{G}})(\beta_j-\beta_{\mathrm{G}})w(r_{i,j}), \tag{5}$$

where $\alpha,\beta\in\{x,y,z\}$ and $\lambda_1\leqslant\lambda_2\leqslant\lambda_3$.

In the second-order MLS method, a curved surface is fitted to the particle positions by minimizing

$$\Lambda_2(\mathbf{r}_i)=\frac{1}{w_0}\sum_j\left[\frac{1}{2}\{C_1X_j^2+C_2Y_j^2\}-Z_j\right]^2 w(r_{i,j}), \tag{6}$$

where X_j, Y_j, and Z_j are the components of the vector $\mathbf{r}_j-\mathbf{r}_0$ in the orthonormal basis $\mathbf{e}_X$, $\mathbf{e}_Y$, and $\mathbf{e}_Z$, respectively. The axis $\mathbf{e}_Z$ is normal to the surface at $\mathbf{r}_0$. The axes $\mathbf{e}_X$ and $\mathbf{e}_Y$ are tangential to the surface at $\mathbf{r}_0$ and are chosen to satisfy $\Sigma_j X_j Y_j w(r_{i,j})=0$. Eight parameters, $\mathbf{r}_0$, C_1, C_2, and the axes, have to be fitted in this case. We do not know an analytical solution of this minimization problem, and Λ_2 can have multiple local minima. Thus, we solve it approximately by using the results of the first-order MLS method. The normal vector of the second-order MLS method is close to that in first-order MLS method, when the radius of curvature is much larger than the average distance of the weight $w(r_{i,j})$. We employ the Monge representation, $z=h(x,y)$, with z axis parallel to $\mathbf{u}_1$. The origin is the weighted center of mass $\mathbf{r}_{\mathrm{G}}$. Equation (6) is then approximated as

$$\Lambda_2^*(\mathbf{r}_i)=\frac{1}{w_0}\sum_j\left(z_0+h_xx_j+h_yy_j+\frac{1}{2}h_{xx}x_j^2+\frac{1}{2}h_{yy}y_j^2+h_{xy}x_jy_j-z_j\right)^2 w(r_{i,j}), \tag{7}$$

where the coefficients z_0, h_x, h_y, h_{xx}, h_{yy}, and h_{xy} of the Taylor expansion are fitting parameters. The minimization of Λ_2^* is obtained as usual by a least-squares fit, which implies a simultaneous solution of five linear equations with $z_0=-(1/w_0)\Sigma_j h_{xx}x_j^2+h_{yy}y_j^2+h_{xy}x_jy_j$. The mean curvature $H_i=(C_1+C_2)/2$ and the Gaussian curvature $K_i=C_1C_2$ are given then by [48]

$$H_i=\frac{(1+h_x^2)h_{yy}+(1+h_y^2)h_{xx}-2h_xh_yh_{xy}}{2(1+h_x^2+h_y^2)^{3/2}}$$

$$K_i=\frac{h_{xx}h_{yy}-h_{xy}^2}{(1+h_x^2+h_y^2)^2}. \tag{8}$$

2. Model I: Curvature potential based on the second-order MLS method

On the basis of the second-order MLS method, we define the curvature potential

$$U_{\mathrm{mls2}}=2k_{\mathrm{cv2}}\sum_i H_i^2+\frac{k_{\mathrm{prt}}}{\sigma^2}\sum_i\Lambda_2^*(\mathbf{r}_i), \tag{9}$$

where $\Lambda_2^*(\mathbf{r}_i)$ and H_i are calculated from Eqs. (7) and (8) after the minimization of $\Lambda_2^*(\mathbf{r}_i)$. The first term is the discretized version of the curvature energy with $k_{\mathrm{cv2}}=\kappa A/N$, where A is the total surface area of membrane. The second term suppresses the particle protrusion from MLS surface. Without the second term, particles assemble not into a membrane, but into a three-dimensional aggregate. For example, in a symmetrical crystal structure, the mean curvature H_i is always zero.

The advantage of this potential is the straightforward discretization of the curvature energy. However, this potential is rather complicated and numerically time consuming, because it requires the inversion of a 5×5 matrix. Since it is difficult to calculate the derivative of this potential, this potential can be employed only in Monte Carlo simulations.

3. Model II: Curvature potential based on the aplanarity

The first-order MLS method does not represent the membrane curvature explicitly. However, the deviation from a plane, $\Lambda_1^{\min}=\lambda_1$, is caused by both membrane curvature and protrusions. We can therefore define a curvature potential $U_{\mathrm{mls1}}=k_1\Sigma_i\lambda_1(\mathbf{r}_i)$. The eigenvalue λ_1 is the smallest solution of the cubic equation $\lambda^3-T_{\mathrm{w}}\lambda^2+M_{\mathrm{w}}\lambda-D_{\mathrm{w}}=0$, where D_{w} and T_{w} are determinant and trace of the gyration tensor (5), respectively, and M_{w} is the sum of its three minors, $M_{\mathrm{w}}=a_{xx}a_{yy}+a_{yy}a_{zz}+a_{zz}a_{xx}-a_{xy}^2-a_{yz}^2-a_{zx}^2$. This equation can be solved analytically. However, λ_1 is C^0 continuous and its derivative is still complicated. When the eigenvalues are degenerated with $\lambda_1=\lambda_2$, its derivative is discontinuous and $\mathbf{n}$ can be an arbitrary unit vector in the plane normal to $\mathbf{u}_3$.

To simplify the potential, we propose a different shape parameter, the aplanarity

$$\alpha_{\rm pl} = 9D_{\rm w}/T_{\rm w}M_{\rm w} = \frac{9\lambda_1\lambda_2\lambda_3}{(\lambda_1+\lambda_2+\lambda_3)(\lambda_1\lambda_2+\lambda_2\lambda_3+\lambda_3\lambda_1)}. \tag{10}$$

The aplanarity $\alpha_{\rm pl}$ takes values in the interval $[0,1]$ and represents the degree of deviation from a plane. It is proportional to λ_1 for $\lambda_1 \ll \lambda_2, \lambda_3$, where $\alpha_{\rm pl} \simeq 9\lambda_1/(\lambda_2+\lambda_3)$. The aplanarity $\alpha_{\rm pl}$ is directly obtained from $D_{\rm w}$, $T_{\rm w}$, and $M_{\rm w}$, and it is not necessary to calculate the eigenvalues. Its derivative is also easy to calculate. The aplanarity is one of the invariants of the gyration tensor (5), like the radius of gyration $R_{\rm g}^2 = T_{\rm w}$ and the asphericity $\alpha_{\rm sp} = 1 - 3M_{\rm w}/T_{\rm w}^2$ [49,50].

Thus, the potential of model II is given by

$$U_\alpha = k_\alpha \sum_i \alpha_{\rm pl}(\mathbf{r}_i), \tag{11}$$

where $\alpha_{\rm pl}(\mathbf{r}_i)=0$ when the ith particle has two or less particles within the cutoff distance $r_{i,j} < r_{\rm cc}$. This potential is smooth except for the case of a particle, which has three neighbor particles with $r_{i,j}=r_{\rm cc}$ at the same time. In practice, this situation never occurs. Thus, the potential (11) is numerical stable.

C. Saddle-splay modulus $\bar{\kappa}$

The calculation of the saddle-splay modulus $\bar{\kappa}$ is not easy in simulations of atomistic and coarse-grained membrane models. A method to estimate $\bar{\kappa}$ in such models from configurational averages of interparticle distances and pair interactions has been proposed in Ref. [51], but has not been employed in simulations thus far. Triangulated-network models have the advantage that the saddle-splay modulus is an explicit parameter and is therefore known exactly [18,28].

Here, we estimate the scale of $\bar{\kappa}$ of our meshless models. In the model I, the saddle-splay modulus should be very small, since the energy is based directly on a discretized mean curvature, and the potential of the protrusion hardly contributes to $\bar{\kappa}$. When a Gaussian curvature potential $\bar{k}_{\rm cv2}\Sigma_i K_i$ is added to the potential $U_{\rm mls2}$, the Gaussian bending rigidity can likely be controlled, with $\bar{k}_{\rm cv2} \simeq \bar{\kappa}\langle A\rangle/N$.

In model II, the aplanarity is approximately $\alpha_{\rm pl} \sim \lambda_1$ for $\lambda_1 \ll \lambda_2, \lambda_3$. In the absence of particle protrusions, a membrane configuration in the Monge representation (compare Sec. II B 1) can be written as

$$z = z_0 + \tfrac{1}{2}C_1(x-x_0)^2 + \tfrac{1}{2}C_2(y-y_0)^2, \tag{12}$$

where a membrane-based reference system is chosen with the principal axes of the curvature tensor and the normal vector as the coordinate system. By averaging over the local neighborhood with a Gaussian weight function $w(r)$ where $r^2=x^2+y^2$, we arrive at

$$\lambda_1 = \langle z^2\rangle - \langle z\rangle^2 = (C_1^2+C_2^2)\langle (r^2 - \langle r^2\rangle)^2\rangle. \tag{13}$$

Since $C_1^2+C_2^2=(C_1+C_2)^2-2C_1C_2$, the saddle-splay modulus of model II should be negative with $\bar{\kappa} \simeq -2\kappa$.

D. Attractive and repulsive potentials

The particles interact with each other in the quasi-two-dimensional membrane surface via

$$U_{\rm iso} = \varepsilon\left\{\sum_{i<j} U_{\rm rep}(r_{i,j}) + \sum_i U_{\rm att}(\rho_i)\right\}. \tag{14}$$

The particles have an excluded volume via the repulsive potential

$$U_{\rm rep}(r_{i,j}) = \exp[-20(r_{i,j}/\sigma - 1) + B] f_{\rm cut}(r_{i,j}/\sigma), \tag{15}$$

where the cutoff function $f_{\rm cut}$ is employed with $n=12$, $A=1$, and $s_{\rm cut}=1.2$. The constant $B=0.126$ is introduced to satisfy $U_{\rm rep}(\sigma)=1$.

A solvent-free membrane model requires an attractive interaction, which mimics the "hydrophobic" repulsion between the hydrocarbon chains of the lipid or surfactant molecules and the aqueous solvent. We employ a potential $U_{\rm att}(\rho_i)$ of the local density of particles

$$\rho_i = \sum_{j\neq i} f_{\rm cut}(r_{i,j}/\sigma), \tag{16}$$

with $n=12$, $s_{\rm half}=r_{\rm att}/\sigma$, and $s_{\rm cut}=s_{\rm half}+0.3$. $\rho_{i,j}$ is the number of particles in the sphere whose radius is approximately $r_{\rm att}$. The potential $U_{\rm att}(\rho_i)$ is defined by

$$U_{\rm att}(\rho_i) = 0.25\ln[1+\exp\{-4(\rho_i-\rho^*)\}] - C, \tag{17}$$

where $C=0.25\ln\{1+\exp(4\rho^*)\}$ is chosen such that $U_{\rm att}(0)=0$. This implies

$$\frac{dU_{\rm att}(\rho_i)}{d\rho_i} = \frac{1}{[1+\exp\{4(\rho_i-\rho^*)\}]}.$$

For $\rho_i < \rho^*$, $U_{\rm att}(\rho_i) \simeq -\rho_i$ and $U_{\rm att}$ acts like a pair potential with $\Sigma_i U_{\rm att}(\rho_i) \simeq \Sigma_{i<j} 2f_{\rm cut}(r_{i,j}/\sigma)$. For $\rho_i > \rho^*$, $U_{\rm att}(\rho_i)$ saturates to the constant $-C$. Thus, this is a pairwise potential with cutoff at higher densities than ρ^*. It is one of the simplest multibody potentials; similar potentials have been employed in other solvent-free membrane [29,30,37] and protein models [52].

In the membrane model of Ref. [30], this multibody potential was employed in order to enhance the molecular diffusion in the membrane and to obtain a wide range of stability of a fluid phase. In the current model, there is an additional reason for employing a density cutoff, which is the suppression of three-dimensional aggregates. For example, the particles have 12 nearest neighbors in a face-centered cubic crystal, while the particles have only six nearest neighbors in a two-dimensional (2D) hexagonal crystal. The density cutoff ρ^* retains the attraction for two-dimensional aggregates, but inhibits additional attractions for three-dimensional aggregates. With pairwise attraction potentials only, the suppression of three-dimensional structures would require a much stronger curvature potential than for the multibody potential (17), which implies that the membrane would have a very large bending rigidity κ. It will be shown in Sec. III below that the density-dependent potential allows a wide range of bending rigidities κ of the membrane.

To chose the parameters of the potentials, information about the crystal structure of the ground state (at temperature

$T=0$) is helpful. The two-dimensional system can have two types of crystal structure, hexagonal and square lattices. The hexagonal crystal has six nearest neighbors and six next-nearest neighbors at distances r_{1n} and $r_{2n}=\sqrt{3}r_{1n}$, respectively. The square crystal has four nearest neighbors and four next-nearest neighbors with $r_{2n}=\sqrt{2}r_{1n}$. For example, the ground state for a square-well (or Heaviside) potential

$$U_{\mathrm{wl}}(r_{i,j})=\begin{cases}\infty & r_{i,j}\leqslant\sigma\\ -1 \quad \text{for} & \sigma<r_{i,j}\leqslant r_{\mathrm{att}}\\ 0 & r_{\mathrm{att}<\mathrm{r_{i,j}}}\end{cases} \tag{18}$$

is a square lattice for $\sqrt{2}<r_{\mathrm{att}}/\sigma<\sqrt{3}$ and hexagonal lattice otherwise. For our potential (14) with $\rho^*=\infty$ (pairwise interactions), the ground state is a square lattice for $1.578<r_{\mathrm{att}}/\sigma<1.841$ and a hexagonal lattice otherwise. As ρ^* decreases, the region of fluid phase increases and particle diffusion in fluid membrane becomes faster. We use mainly the parameters $r_{\mathrm{att}}/\sigma=1.8$ and $\rho^*=6$. We also use $r_{\mathrm{att}}/\sigma=1.9$ and $\rho^*=8$ to show robustness of the results to the choice of parameters.

E. Simulation methods: Brownian dynamics and Monte Carlo

We simulated the membrane in the NVT (constant particle number, volume, and temperature) ensemble with a simulation box of fixed size and shape. In the Monte Carlo (MC) simulations of model I, random movements of particles are accepted or rejected according to the Metropolis scheme. The distance of the particle displacements is adjusted to obtain roughly a 50% acceptance ratio.

In the Brownian dynamics (BD) simulations of model II, the motion of particles is determined by the underdamped Langevin equations

$$m\frac{d^2\mathbf{r}_i}{dt^2}=-\frac{\partial U}{\partial\mathbf{r}_i}-\zeta\frac{d\mathbf{r}_i}{dt}+\mathbf{g}_i(t), \tag{19}$$

where m is the mass of a particle and ζ the friction constant. $\mathbf{g}_i(t)$ is a Gaussian white noise, which obeys the fluctuation-dissipation theorem

$$\langle g_{i,\alpha}(t)\rangle=0,$$

$$\langle g_{i,\alpha}(t)g_{j,\beta}(t')\rangle=2k_{\mathrm{B}}T\zeta\delta_{ij}\delta_{\alpha\beta}\delta(t-t'), \tag{20}$$

where $\alpha,\beta\in\{x,y,z\}$ and $k_{\mathrm{B}}T$ is the thermal energy. In the following, we chose the time unit $\tau=\zeta\sigma^2/k_{\mathrm{B}}T$ and the energy unit $k_{\mathrm{B}}T$. We used $m=\zeta\tau$. The diffusion constant of an isolated particle is $D_0=\sigma^2/\tau$. The equations are integrated by the leapfrog algorithm with a time step of $\Delta t=0.005\tau$ [53]. Brownian dynamics simulations of model II are roughly 20 times faster than Monte Carlo simulations of model I with respect to particle diffusion.

We simulated the membrane with periodic boundary conditions in a box of dimensions $L_x\times L_y\times L_z$. To calculate equilibrium properties, a nearly planar membrane perpendicular to the z direction with $L_x=L_y$ or an isolated vesicle is employed, where all particles belong to the membrane, i.e., no monomers are found outside the membrane. For comparison, we also investigate a two-dimensional (2D) system (without the curvature potentials), which corresponds to a membrane with infinite bending rigidity. The error bars of the data are estimated from the standard deviations of three independent runs.

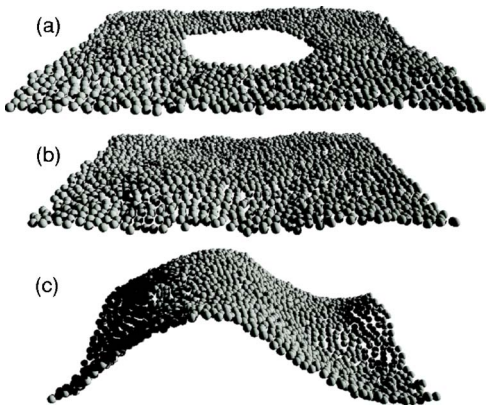

FIG. 2. (Color online) Snapshots of membranes with $N=1600$ particles, $k_\alpha/k_{\mathrm{B}}T=10$, $\varepsilon/k_{\mathrm{B}}T=4$, $r_{\mathrm{att}}/\sigma=1.8$, and $\rho^*=6$. (a) A pore-opened membrane with projected area (in the xy plane) per particle of $A_{xy}/(N\sigma^2)=1.65$. (b) A tensionless, nearly planar membrane ($\gamma=0$) with $A_{xy}/(N\sigma^2)=1.4197$. (c) A buckled membrane with $A_{xy}/(N\sigma^2)=1.25$.

III. RESULTS AND DISCUSSION

A. Relaxation dynamics: Models I and II

Both models I and II form membranes and show similar dynamics. As the temperature decreases, the particles self-assemble into membranes. The resulting shapes are vesicles or nearly planar membranes depending on the simulation-box size and the particle density. This behavior is similar to that observed in the bilayer model of Ref. [30]. As k_α or k_{prt} increases, the particles form vesicles from a three-dimensional spherical aggregate. Thus, the three-dimensional aggregate is not even a metastable state. As the temperature increases, a pore opens in a vesicle and particles dissolve from the pore edge. A similar "opening-up" dynamics was observed experimental in the lysis of liposomes with detergents [54]. The details of dynamic behavior of our model will be reported elsewhere.

B. Membrane elasticity and fluctuations: Model II with $r_{\mathrm{att}}/\sigma=1.8$ and $\rho^*=6$

We mainly employ model II with an attractive potential U_{att} with the parameters $r_{\mathrm{att}}/\sigma=1.8$ and $\rho^*=6$ in this paper. We simulate nearly planar membrane with various projected areas $A_{xy}=L_xL_y$ to investigate the membrane properties. Surface tension γ, intrinsic area A, diffusion constant D, and bending rigidity κ are calculated from membrane configurations without pores [see Figs. 2(b) and 2(c)]. The line tension Γ is calculated from the stretched membrane with a pore [see Fig. 2(a)].

The surface tension γ is given by [34,53,55]

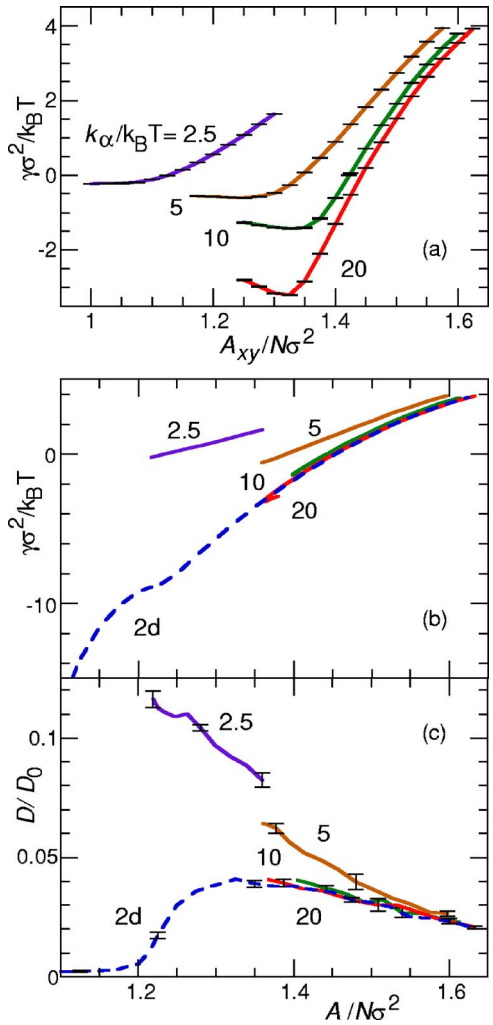

FIG. 3. (Color online) Area dependence of (a),(b) the surface tension γ and (c) the diffusion constant D, for various k_α at $\varepsilon/k_BT=4$, $N=400$, $r_{att}/\sigma=1.8$, and $\rho^*=6$. The data for γ are shown as a function of (a) the intrinsic area A and (b) the projected area A_{xy}, respectively. The curves are labeled by their k_α/k_BT values. The dashed lines represent the data in the two-dimensional case ($k_\alpha=\infty$). Error bars are shown for (a) all, (b) none, and (c) several data points.

$$\gamma = \langle P_{zz} - (P_{xx} + P_{yy})/2 \rangle L_z, \tag{21}$$

with the diagonal components of the pressure tensor

$$P_{\alpha\alpha} = \left(N k_B T - \sum_i \alpha_i \frac{\partial U}{\partial \alpha_i} \right) / V, \tag{22}$$

where $\alpha \in \{x, y, z\}$. The form (22) of the pressure tensor is appropriate for multibody potentials, such as our potentials U_{att} and U_α. It can be shown easily that it reduces to the standard form for pair potentials. Note that in solvent-free models, the pressure P_{zz} perpendicular to the membrane is determined by the density of monomers outside the membrane and is therefore very small. Figures 3 and 4 show the area dependence of γ and D. For $\gamma \leqslant 0$, the intrinsic area A is larger than the projected area A_{xy} in the xy plane due to the membrane undulations. We calculate A from a

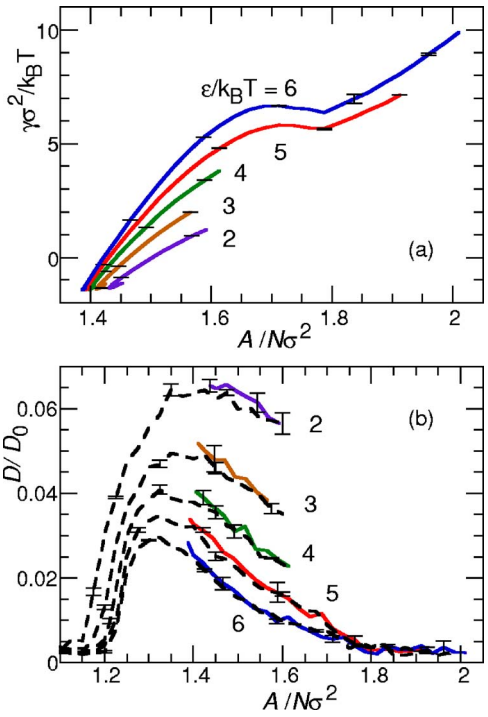

FIG. 4. (Color online) Area A dependence of (a) the surface tension γ and (b) the diffusion constant D, for various ε at $k_\alpha/k_BT=10$. The other parameters are the same as in Fig. 3. The curves are labeled by their ε/k_BT values. The dashed lines in (b) represent the data in the two-dimensional case. Error bars are shown at several data points.

$\sqrt{N}\times\sqrt{N}$ square mesh with $(x_{mh}, y_{mh}) = (d_{mh}i, d_{mh}j)$. The height z_{mh} of a mesh point is obtained from a weighted average of particles in the four neighbor cells, with $z_{mh} = \Sigma_i z_i w_{mh}(x_i, y_i) / [\Sigma_i w_{mh}(x_i, y_i)]$ and $w_{mh}(x_i, y_i) = (1 - |x_i - x_{mh}|/d_{mh})(1 - |y_i - y_{mh}|/d_{mh})$. The diffusion constant D of particles is calculated from the diffusion of the particle projections in the xy plane, $D = \langle [x_i(t) - x_i(0)]^2 + [y_i(t) - y_i(0)]^2 \rangle / 4t$.

As A_{xy} decreases, the surface tension γ first decreases roughly linearly, then levels off [compare Fig. 3(a)] when the membrane buckles out of plane [see Fig. 2(c)]. The intrinsic area A does not exhibit this saturation [Fig. 3(b)]. We will discuss the buckling behavior in more detail in Sec. III D. The diffusion constant [see Fig. 3(c)] is indistinguishable from the two-dimensional limit for $k_\alpha/k_BT \geqslant 10$, and becomes faster at smaller k_α. The lines in Figs. 3 and 4 end for large A at the maximum area before a pore opens. The fluid phase is obtained for $1.2 \lesssim A/(N\sigma^2) \lesssim 1.8$; a crystalline or hexatic phase is obtained at smaller or larger membrane areas A. Around the transition area, γ shows a van der Waals-type loop, in agreement with previous results of two-dimensional melting simulations [56]. The transition area is not sensitive to ε. Since our main interest is the fluid phase, we have not investigated the crystalline and hexatic phases in any further detail.

As k_α decreases or ε increases, γ increases [see Figs. 3(b) and 4(a)] and the area A_0 of the tensionless membrane decreases [compare Figs. 5(a) and 6(a)]. This behavior is

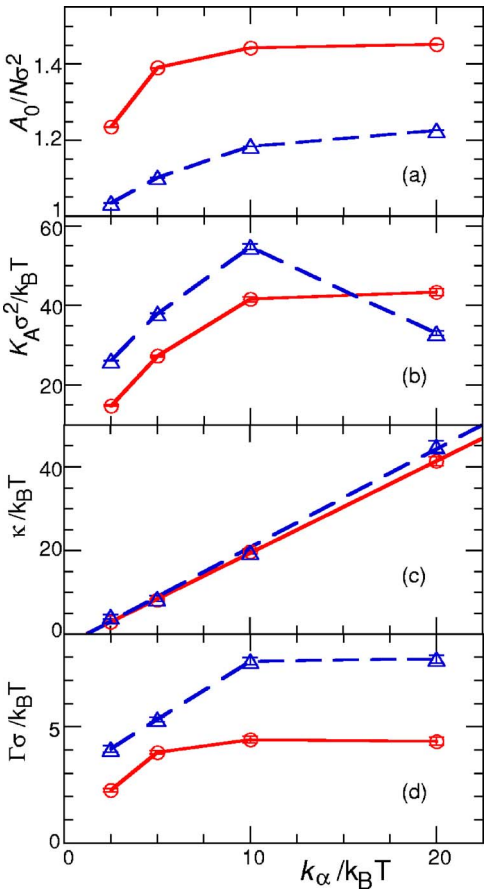

FIG. 5. (Color online) Parameter k_α dependence of (a) the area A_0, (b) the area compression modulus K_A, (c) the bending rigidity κ, and (d) the line tension Γ, for $\varepsilon/k_BT=4$. The data in (a)–(c) are calculated at $\gamma=0$. The solid lines represent data for $r_{att}/\sigma=1.8$ and $\rho^*=6$. The dashed lines represent data for $r_{att}/\sigma=1.9$ and $\rho^*=8$. Solid and dashed lines in (c) show linear fits, $\kappa/k_BT=2.2k_\alpha/k_BT-2.5$ and $\kappa/k_BT=2.35k_\alpha/k_BT-2.8$, respectively.

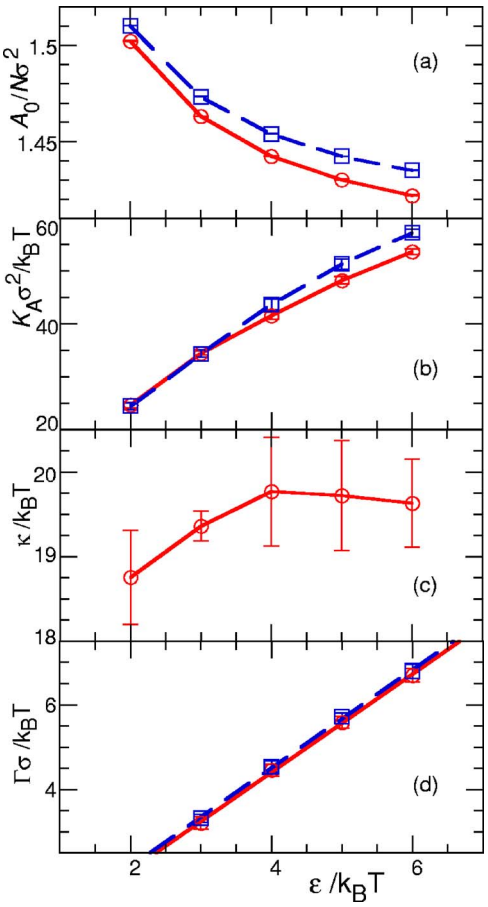

FIG. 6. (Color online) Parameter ε dependence of (a) the area A_0/N per particle, (b) the area compression modulus K_A, (c) the bending rigidity κ, and (d) the line tension Γ, for $r_{att}/\sigma=1.8$ and $\rho^*=6$. The data in (a)–(c) are calculated at $\gamma=0$. The solid and dashed lines represent data for $k_\alpha/k_BT=10$ and the two-dimensional system, respectively. Solid and dashed lines in (d) show linear fits, $\Gamma\sigma/k_BT=1.16\varepsilon/k_BT-0.22$ and $\Gamma\sigma/k_BT=1.16\varepsilon/k_BT-0.13$, respectively.

caused by larger out-of-plane particle protrusions (for decreasing k_α) or denser in-plane particle packing (for increasing ε). The area compression modulus K_A is defined by

$$K_A = A_0 \partial\gamma / \partial A|_{A=A_0}. \tag{23}$$

As k_α or ε increases, K_A increases, i.e., the area fluctuations decrease. In the case of increasing k_α this is due to the reduction of protrusions, in the case of increasing ε to stronger in-plane particle interactions, which reduce the fluctuations of the nearest-neighbor distances.

The bending rigidity κ is calculated from the spectrum of undulation modes $\langle|h(q)|^2\rangle$ of nearly planar membranes in Fourier space [57],

$$\langle|h(q)|^2\rangle = \frac{k_BT}{\gamma q^2 + \kappa q^4}. \tag{24}$$

Figure 7 clearly shows the q^{-4} dependence of the tensionless membrane ($\gamma=0$). We calculate $|h(q)|^2$ from the raw data (the positions of particles), as well as on a square mesh with the same mesh points that were employed for the estimation of the internal area A. The averaging on the mesh removes most of the effects of the particle protrusions. We estimate κ and γ from a fit of $1/\langle|h(q)|^2\rangle=(\gamma/k_BT)q^2+(\kappa/k_BT)(q^2)^2$ for $N=1600$ [see inset of Fig. 7]. Figure 8 shows the results of these fits. The values of γ extracted from $\langle|h(q)|^2\rangle$ agree very well with those obtained from the pressure tensor Eq. (21) [see Fig. 8(b)]. We used γ estimated from the pressure tensor to calculate K_A and A_0, since its statistical error is smaller. The bending rigidity κ is found to be almost independent of the intrinsic membrane area A. A weak area dependence of κ was reported in molecular simulations of monolayer membranes at liquid-liquid interfaces [58]. A model in which κ is essentially independent of the area per molecule is certainly to be preferred in studies of the general properties of membranes.

We also estimate the bending rigidity κ from the fluctuations of quasi-spherical vesicles to check consistency. The vesicle shape is described in spherical coordinates (θ,φ) by a series of spherical harmonics $Y_{l,m}(\theta,\varphi)$. The distance between particles and the center of mass of the vesicle is then

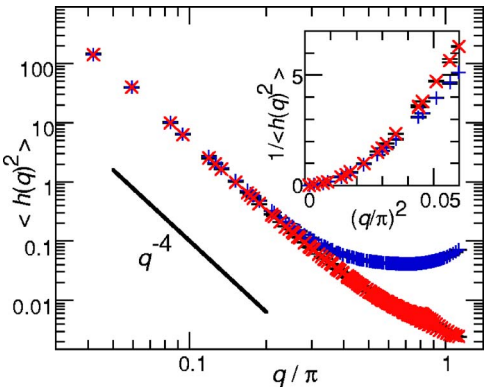

FIG. 7. (Color online) Spectra of undulation modes $\langle|h(q)|^2\rangle$ of nearly planar, tensionless membranes ($\gamma=0$). The parameters are the same as in Fig. 2(b). Results for $\langle|h(q)|^2\rangle$ calculated from the particle positions (+) and from the averaged positions on a square mesh (×) are shown. The inset shows the dependence of $1/\langle|h(q)|^2\rangle$ on q^2, which is used to extract the surface tension γ and the bending rigidity κ.

given by $r(\theta,\varphi)=R_0[1+\Sigma_{l,m}u_{l,m}Y_{l,m}(\theta,\varphi)]$. Here, $R_0=\sqrt{A/4\pi}$ is the radius of a sphere of equal surface area, which is calculated from the average density $\langle\rho_i\rangle$ and area-density relation. The density $\langle\rho_i\rangle$ in Eq. (16) and $\langle w_0\rangle$ in Eq. (4) are linearly dependent on A for nearly planar membrane [data not shown]. The power spectrum of undulations is given by [59–61]

$$\langle u_{l,m}^2\rangle = \frac{k_BT}{\kappa(l-1)l(l+1)(l+2)}. \tag{25}$$

Figure 9 shows the effective bending rigidity derived from $\langle u_{l,m}^2\rangle$ at $k_\alpha/k_BT=10$ and $\varepsilon/k_BT=4$. For the two larger vesicle sizes, Eq. (25) implies $\kappa/k_BT=22\pm2$, is in good agreement with the value $\kappa/k_BT=19.8\pm0.6$ calculated from $\langle|h(q)|^2\rangle$ of nearly planar membranes in the tensionless state. The decrease of the effective bending rigidity in Fig. 9 with increasing l for small vesicle size ($N=500$) might be caused by membrane protrusion or higher-order term of curvature elastic energy in Eq. (1).

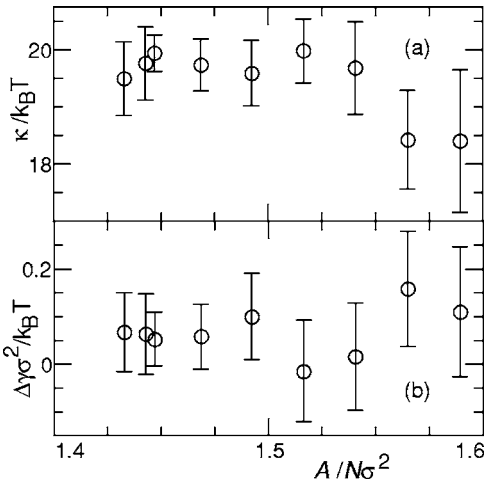

FIG. 8. Area A dependence of (a) bending rigidity κ and (b) the difference $\Delta\gamma=\gamma_1-\gamma_0$ in estimating the surface tension from Eqs. (24) and (21), respectively. The parameters are the same as in Fig. 2.

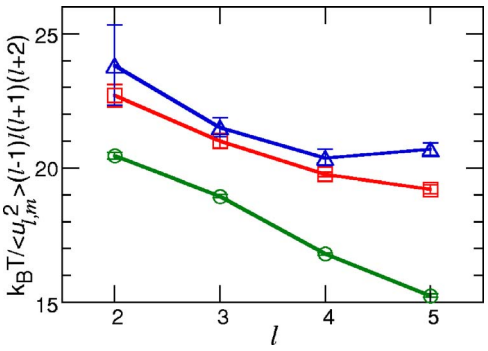

FIG. 9. (Color online) Estimation of bending rigidity κ from the power spectra $u_{l,m}^2$ of spherical harmonics of quasi-spherical vesicles. Circles, squares, and triangles represent the data for $N=500$, 2000, and 8000, respectively. The other parameters are the same as in Fig. 2.

The elastic energy of a planar membrane with a circular pore of radius r_{p0} at constant $\gamma>0$ is given by

$$G = \gamma(A_{xy} - \pi r_{p0}^2) + 2\pi\Gamma r_{p0} \tag{26}$$

in the range of γ, where circular pores are stable, the excess area $A-A_{xy}$ is very small and can therefore be neglected. From $\partial G/\partial r_{p0}|_\gamma=0$, the line tension Γ is found to be

$$\Gamma = \gamma r_{p0}. \tag{27}$$

The same relation is obtained in an ensemble of constant preferred area A_0 and area compressibility K_A. In this case, the elastic energy reads [33,62]

$$F = \frac{K_A}{2A_0}(A_{xy} - \pi r_{p0}^2 - A_0)^2 + 2\pi\Gamma r_{p0}. \tag{28}$$

Differentiation with respect to the pore radius reproduces Eq. (27) with $\gamma=K_A(A-A_0)/A_0$. The surface tension γ is calculated in the membrane region further away than 5σ from the pore edge via the pressure tensor, Eq. (21).

We estimate the radius of the pore by two methods. In the first method, we determine the membrane area A from the calculated surface tension γ in Figs. 3 and 4(a) [see also Fig. 14 below]. Then, the radius is given by $r_{p0}=\sqrt{(A_{xy}-A)/\pi}$. We use this radius r_{p0} to calculate Γ. In the second method, we directly estimate the pore area A_{p1} by employing the Monte Carlo method proposed by Tolpekina *et al.* [62]. Ghost particles with hard-sphere diameter σ are distributed randomly in the xy space; the particle placement is accepted if no overlap with the projections of the hard cores of the membrane particles occurs. The area covered by the centers of the ghost particles is obtained as $A_{p1}=A_{xy}\nu$, where ν is the acceptance ratio of particles insertion. Finally, the radius of the hole is given by $r_{p1}=\sqrt{A_{p1}/\pi}+\sigma/2$. The line tension is found to be independent of the radius r_{p0}, and the two radii r_{p0} and r_{p1} coincide very well, as shown in Fig. 10. The radius r_{p0} is employed for the Γ estimation in Eq. (27), since

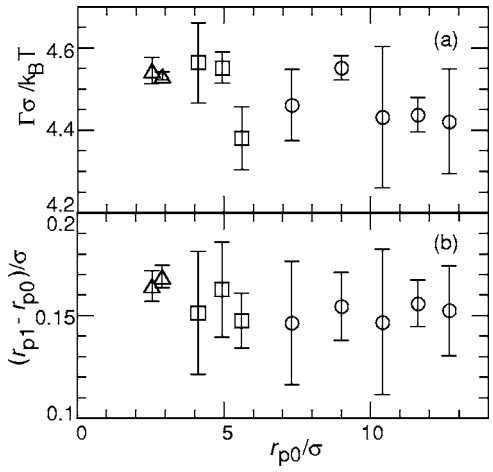

FIG. 10. Estimation of the line tension Γ of pore-opened nearly planar membranes from the data at various area A_{xy}. The pore radius r_{p0} and r_{p1} are calculated from the γ–A_{xy} relation and the particle-insertion method, respectively. Data are shown for three different system sizes, $N=100$ (△), $N=400$ (□), and $N=1600$ (○). The other parameters are the same as in Fig. 2.

this definition is consistent with Eq. (26). We use the average of the data for $N=1600$ to determine the line tension Γ.

The bending rigidity κ is linearly dependent on k_α and almost independent of ε. On the other hand, the line tension Γ is linearly dependent on ε and almost independent of k_α for $k_\alpha/k_BT>5$ [see Figs. 5 and 6]. Thus, κ and Γ can be controlled independently by varying k_α and ε, respectively.

C. Membrane elasticity and fluctuations: Model II with $r_{att}/\sigma=1.9$ and $\rho^*=8$

Figure 11 shows the surface tension γ and diffusion constant D of a nearly planar membrane with $r_{att}/\sigma=1.9$ and $\rho^*=8$. A membrane with this parameter set has a transition between a hexatic (or crystalline) and a fluid phase at $\gamma\simeq 0$ for $k_\alpha/k_BT\geqslant 20$. This parameter set can therefore be employed to study the effect of membrane undulations on the crystalline-to-fluid phase transitions. The region of stability of the fluid phase can be varied by the choice of the parameters r_{att}/σ and ρ^*.

The ε dependence of the equilibrium properties is similar to the membrane with $r_{att}/\sigma=1.8$ and $\rho^*=6$, as shown in Fig. 5. The decrease of K_A from $k_\alpha/k_BT=10$ to 20 is caused by the van der Waals loop of the phase transition (see Fig. 11). The bending rigidity κ is determined by the curvature potential U_α and is found to be almost independent of U_{att}, since the deviation of the two lines in Fig. 5(c) is very small. The membrane with $r_{att}/\sigma=1.9$ and $\rho^*=8$ also shows k_α dependences similar to the membrane with $r_{att}/\sigma=1.8$ and $\rho^*=6$ [data not shown]. Thus, the dependence of κ and Γ on k_α and ε is not sensitive to the detailed form of the attractive potential U_{att}.

D. Finite-size effects

The intrinsic membrane area A is larger than its projected area A_{xy} due to membrane undulations and particle protrusions. The ratio of excess area and projected area can be derived from Eq. (24) to be

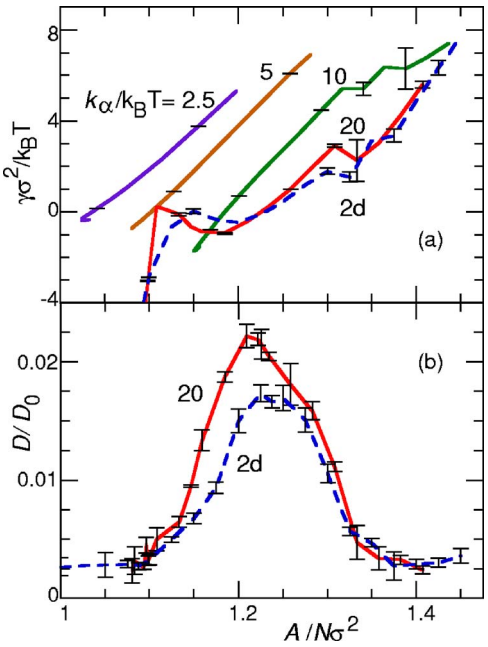

FIG. 11. (Color online) Area A dependence of (a) the surface tension γ and (b) the diffusion constant D, for various k_α at $\varepsilon/k_BT=4$, $N=400$, $r_{att}/\sigma=1.9$, and $\rho^*=8$. The curves are labeled by the corresponding k_α/k_BT values. The dashed lines represent the data for the two-dimensional systems. Error bars are shown for (a) several and (b) all data points.

$$\frac{A-A_{xy}}{A_{xy}}=\frac{1}{2A_{xy}}\sum_{i,j}q_{i,j}^2\langle h(q_{i,j})^2\rangle+b_{prt}$$

$$=\frac{1}{8\pi^2}\sum_{i,j}\frac{T}{\gamma A_{xy}/4\pi^2+\kappa(i^2+j^2)}+b_{prt}, \qquad (29)$$

where the summation includes $-\sqrt{N}/2<i,j\leqslant\sqrt{N}/2$, except for $i=j=0$. The contribution of the protrusion b_{prt} is assumed to be independent of γ and N. For $\gamma=0$, the undulation contribution to Eq. (29) can be approximated as $\ln(aN)/8\pi\kappa$, where $a=0.71$ is a fitting parameter [63,64]. Then, the excess area ratio at $\gamma=0$ is given by

$$\frac{A-A_{xy}}{A_{xy}}=\frac{T}{8\pi\kappa}\ln(0.71N)+b_{prt} \qquad (30)$$

This relation coincides very well with our simulation results as shown in Fig. 12. The fitted values $\kappa=22.0\pm0.3$ and 23.7 ± 0.5 for $r_{att}/\sigma=1.8$ an 1.9 agree quite well with those ($\kappa=19.7\pm0.6$ and 19.5 ± 0.4, respectively) obtained from the undulation spectrum, Eq. (24), given the difficulties in estimating numerical errors.

Figures 13 and 14 show the finite-size effects in the dependence of γ and $A-A_{xy}$ on the intrinsic and projected areas. The data of Fig. 14 for the γ-A relation show no N dependence; data for different N all fall onto a single curve, except for very small A_{xy}. On the other hand, the excess area ratio $(A-A_{xy})/A_{xy}$ shows a strong N dependence for negative

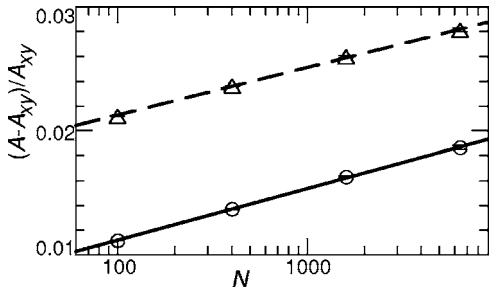

FIG. 12. System-size N dependence of the excess area due to membrane undulations of tensionless ($\gamma=0$) membranes for $k_\alpha/k_BT=10$ and $\varepsilon/k_BT=4$. Data are shown for $r_{att}/\sigma=1.8$ and $\rho^*=6$ (○) and $r_{att}/\sigma=1.9$ and $\rho^*=8$ (△). Solid and dashed lines represent fits to Eq. (30) with $\kappa/k_BT=22.0\pm0.3$ and $b_{prt}=0.0035\pm0.0002$ and $\kappa/k_BT=23.7\pm0.5$ and $b_{prt}=0.0141\pm0.0002$, respectively.

γ. This behavior can be understood on the basis of Eq. (29). At $\gamma=-4\pi^2\kappa/A_{xy}$, the amplitude of the modes with wave number $q=2\pi/L$ diverges. This implies that the nearly planar membrane becomes unstable, the membrane buckles at small A_{xy} [compare Fig. 2], and γ levels off at small A_{xy} as shown in Figs. 3(a) and 13(a). This saturation occurs at smaller negative γ for larger N or smaller κ since $A_{xy}\propto N$.

We estimated this saturation from Eq. (29) and $\gamma=K_A(A-A_0)/A_0$ with the parameter extracted from Fig. 12 [see dashed lines in Fig. 13]. This explains the dependence of γ on A_{xy} almost quantitatively. However, a small deviation remains between the solid and dashed lines for $A_{xy}/(N\sigma^2)<1.35$, since the assumption of thermal undulations around a planar reference state is no longer applies in this region. As

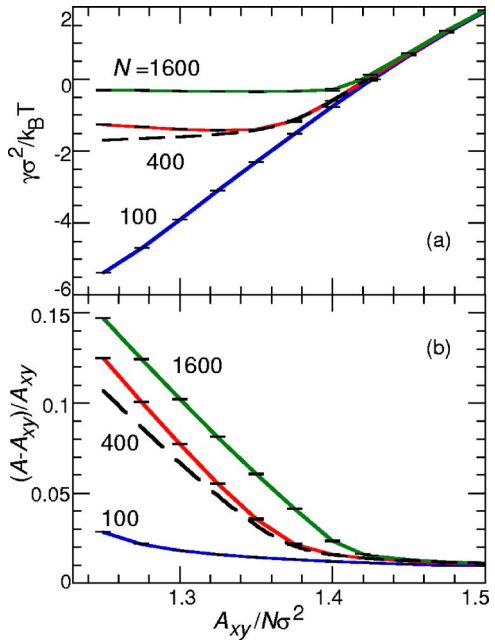

FIG. 13. (Color online) Projected area A_{xy} dependence of (a) the surface tension γ and (b) the undulated area ratio. The numbers given in figure are N. The dashed lines represent data from Eq. (29) with $N=400$. The parameters are the same as in Fig. 2. Error bars are shown at all data points.

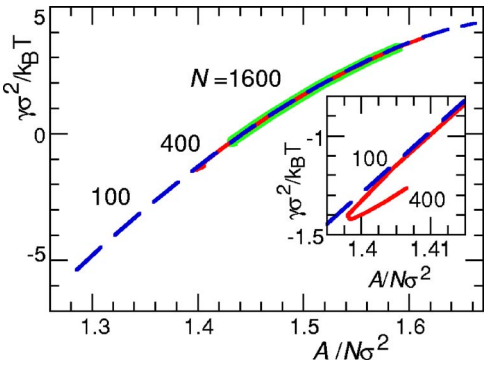

FIG. 14. (Color online) Intrinsic area A dependence of the surface tension γ. The dashed, solid, and thick-green (or gray) lines represent data for $N=100$, 400, and 1600, respectively. The parameters are the same as in Fig. 2. The inset shows the region around $A/(N\sigma^2)=1.4$ in more detail, where A of a buckled membrane is shown to increase with decreasing A_{xy} for $N=400$.

A_{xy} decreases from $A_{xy}/(N\sigma^2)=1.35$ to 1.25 at $N=400$, the intrinsic area $A/(N\sigma^2)$ slightly increases and the magnitude of γ slightly decreases, see Fig. 13. This leads to a little hook in the γ-A relation, as shown in Fig. 14. The additional surface tension is caused by the curvature of the buckled membranes. Similar saturations were reported in some models of bilayers [65,66] and wormlike micelles [67]. On the other hand, it was not observed in other membrane simulations [68,69], since the ranges of area variation were too small in comparison with the employed bending rigidities κ.

The threshold area to open a pore decreases with increasing system size [see Fig. 14]. This agrees with the results of Ref. [62].

IV. SUMMARY AND CONCLUSIONS

We have proposed a meshless membrane model and investigated its equilibrium properties. The model is defined by three interaction potentials, a short-range repulsive interaction, a density-dependent attractive interaction of longer range, and an interaction that favors locally planar conformations of the membrane particles. The strengths of the first two contribution is described by a parameter ϵ, the strength of the third contribution by a parameter k_α. For positive surface tensions, the membrane is first stretched uniformly with increasing γ. Then, the membrane ruptures and a circular hole opens. For negative surface tensions, a buckling instability occurs. The bending rigidity κ and the line tension Γ are obtained from the undulation modes of nearly planar membranes and vesicles and from the free energy of the holes, respectively. We find that κ and Γ depend linearly on the parameters k_α and ε, respectively, but are nearly independent of the other parameter. Thus, bending rigidity and line tension can be controlled independently in our model.

BD and MC of the MLS membrane model do not take into account the solvent explicitly. Thus, hydrodynamic interactions are not taken into account. This does not affect the static equilibrium properties, but is very important when dynamical properties are investigated. It is one of the advan-

tages of solvent-free models that a mesoscale solvent with highly simplified interactions can be easily added to the system, where the role of the solvent particles is only to mimic hydrodynamic behavior. For our meshless membrane model, this can be done straightforwardly by combining it with a mesoscopic solvent technique, such as multiparticle collision dynamics (MPCD) [70]. We have already shown that such an approach works very well in the case of dynamically triangulated surface models of membranes, where the combination with a mesoscale solvent described by MPCD allows the investigation of vesicle dynamics in shear and capillary flows [26,27].

A somewhat different approach has been used by Lenz and Schmid [71] for a coarse-grained membrane model. An ideal-gas solvent was introduced, where the particles interact with the membrane but not with each other, in order to stabilize the membrane. This model was used in MC simulations to study pressure effects on the fluid-gel transition. In such a model, MPCD could also be employed straightforwardly to incorporate hydrodynamic effects.

A further advantage of such models is that hydrodynamic interactions can easily switched on or off in the simulations. Static equilibrium properties can be investigated by BD or MC, which needs much less computational time. Thus, our membrane model should be applicable to study phenomena on scales much larger than the size of a lipid molecule, both in and out of equilibrium, in particular, the effects of topology changes.

[1] S. A. Safran, *Statistical Thermodynamics of Surfaces, Interfaces, and Membranes* (Addison-Wesley, Reading, MA, 1994).
[2] G. Gompper and M. Schick, *Self-Assembling Amphiphilic Systems*, in Phase Transitions and Critical Phenomena Vol. 16 (Academic Press, London, 1994).
[3] *Structure and Dynamics of Membranes*, edited by R. Lipowsky and E. Sackmann (Elsevier Science, Amsterdam, 1995).
[4] U. Seifert, Adv. Phys. **46**, 13 (1997).
[5] O. Diat and D. Roux, J. Phys. II **3**, 9 (1993).
[6] O. Diat, D. Roux, and F. Nallet, J. Phys. II **3**, 1427 (1993).
[7] K. Mortensen, Curr. Opin. Colloid Interface Sci. **6**, 140 (2001).
[8] F. Nettersheim, J. Zipfel, U. Olsson, F. Renth, P. Lindner, and W. Richtering, Langmuir **19**, 3603 (2003).
[9] B. R. Lentz, V. Malinin, M. E. Haque, and K. Evans, Curr. Opin. Struct. Biol. **10**, 607 (2000).
[10] R. Jahn and H. Grubmüller, Curr. Opin. Cell Biol. **14**, 488 (2002).
[11] W. Helfrich, Z. Naturforsch. C **28**, 693 (1973).
[12] F. Jülicher and R. Lipowsky, Phys. Rev. E **53**, 2670 (1996).
[13] T. Umeda, Y. Suezaki, K. Takiguchi, and H. Hotani, Phys. Rev. E **71**, 011913 (2005).
[14] D. P. Tieleman, S. J. Marrink, and H. J. C. Berendsen, Biochim. Biophys. Acta **1331**, 235 (1997).
[15] J. C. Shelley and M. Y. Shelley, Curr. Opin. Colloid Interface Sci. **5**, 101 (2000).
[16] S. O. Nielsen, C. F. Lopez, G. Srinivas, and M. L. Klein, J. Phys.: Condens. Matter **16**, R481 (2004).
[17] G. Gompper and D. M. Kroll, J. Phys.: Condens. Matter **9**, 8795 (1997).
[18] G. Gompper and D. M. Kroll, in *Statistical Mechanics of Membranes and Surfaces*, 2nd ed., edited by D. R. Nelson, T. Piran, and S. Weinberg (World Scientific, Singapore, 2004).
[19] Y. Kantor, M. Kardar, and D. R. Nelson, Phys. Rev. Lett. **57**, 791 (1986).
[20] H. S. Seung and D. R. Nelson, Phys. Rev. A **38**, 1005 (1988).
[21] F. F. Abraham, W. E. Rudge, and M. Plischke, Phys. Rev. Lett. **62**, 1757 (1989).
[22] J.-S. Ho and A. Baumgärtner, Europhys. Lett. **12**, 295 (1990).
[23] D. M. Kroll and G. Gompper, Science **255**, 968 (1992).
[24] D. H. Boal and M. Rao, Phys. Rev. A **45**, R6947 (1992).
[25] M. Kraus, W. Wintz, U. Seifert, and R. Lipowsky, Phys. Rev. Lett. **77**, 3685 (1996).
[26] H. Noguchi and G. Gompper, Phys. Rev. Lett. **93**, 258102 (2004).
[27] H. Noguchi and G. Gompper, Proc. Natl. Acad. Sci. U.S.A. **102**, 14159 (2005).
[28] G. Gompper and D. M. Kroll, Phys. Rev. Lett. **81**, 2284 (1998).
[29] J. M. Drouffe, A. C. Maggs, and S. Leibler, Science **254**, 1353 (1991).
[30] H. Noguchi and M. Takasu, Phys. Rev. E **64**, 041913 (2001).
[31] H. Noguchi and M. Takasu, Biophys. J. **83**, 299 (2002).
[32] H. Noguchi, Phys. Rev. E **67**, 041901 (2003).
[33] O. Farago, J. Chem. Phys. **119**, 596 (2003).
[34] G. Brannigan and F. L. H. Brown, J. Chem. Phys. **120**, 1059 (2004).
[35] G. Brannigan, P. F. Philips, and F. L. H. Brown, Phys. Rev. E **72**, 011915 (2005).
[36] I. R. Cooke, K. Kremer, and M. Deserno, Phys. Rev. E **72**, 011506 (2005).
[37] Z. J. Wang and D. Frenkel, J. Chem. Phys. **122**, 234711 (2005).
[38] F. C. MacKintosh and T. C. Lubensky, Phys. Rev. Lett. **67**, 1169 (1991).
[39] M. Hamm and M. M. Kozlov, Eur. Phys. J. B **6**, 519 (1998).
[40] Y. Kozlovsky and M. M. Kozlov, Biophys. J. **82**, 882 (2002).
[41] N. Amenta and M. Bern, Discrete Comput. Geom. **22**, 481 (1999).
[42] E. G. Flekkoy and P. V. Coveney, Phys. Rev. Lett. **83**, 1775 (1999).
[43] M. Serrano and P. Español, Phys. Rev. E **64**, 046115 (2001).
[44] T. Belytschko, Y. Krongauz, D. Organ, M. Fleming, and P. Krysl, Comput. Methods Appl. Mech. Eng. **139**, 3 (1996).
[45] P. Lancaster and K. Salkaskas, Math. Comput. **37**, 141 (1981).
[46] N. Amenta and Y. J. Kil, ACM SIGGRAPH'04, pp. 264–270 (2004).
[47] F. H. Stillinger and T. A. Weber, Phys. Rev. B **31**, 5262 (1985).
[48] M. Spivak, *A Comprehensive Introduction to Differential Geometry* (Publish or Perish, Houston, 1979), Vol. 3.
[49] J. Rudnick and G. Gaspari, J. Phys. A **19**, L191 (1986).

[50] J. A. Aronowitz and D. R. Nelson, J. Phys. (France) **47**, 1445 (1986).
[51] O. Farago and P. Pincus, J. Chem. Phys. **120**, 2934 (2004).
[52] S. Takada, Z. Luthey-Schulten, and P. G. Wolynes, J. Chem. Phys. **110**, 11616 (1999).
[53] M. P. Allen and D. J. Tildesley, *Computer Simulation of Liquids* (Clarendon, Oxford, 1987).
[54] F. Nomura, M. Nagata, T. Inaba, H. Hiramatsu, H. Hotani, and K. Takiguchi, Proc. Natl. Acad. Sci. U.S.A. **98**, 2340 (2001).
[55] J. S. Rowlinson and B. Widom, *Molecular Theory of Capillarity* (Clarendon, Oxford, 1982).
[56] K. J. Strandburg, Rev. Mod. Phys. **60**, 161 (1988).
[57] W. Helfrich, Z. Naturforsch. A **33**, 305 (1978).
[58] L. Rekvig, B. Hafskjold, and B. Smit, Phys. Rev. Lett. **92**, 116101 (2004).
[59] W. Helfrich, J. Phys. (France) **47**, 321 (1986).
[60] S. T. Milner and S. A. Safran, Phys. Rev. A **36**, 4371 (1987).
[61] In Eq. (9) of Ref. [31], l is missing in the denominator.
[62] T. V. Tolpekina, W. K. den Otter, and W. J. Briels, J. Chem. Phys. **121**, 8014 (2004).
[63] W. Helfrich and R. M. Servuss, Nuovo Cimento Soc. Ital. Fis., D **3**, 137 (1984).
[64] D. Roux, F. Nallet, E. Freyssingeas, G. Porte, P. Bassereau, M. Skouri, and J. Marignan, Europhys. Lett. **17**, 575 (1992).
[65] J. Stecki, J. Chem. Phys. **122**, 111102 (2005).
[66] M. Deserno, private comunication.
[67] W. K. den Otter, S. A. Shkulipa, and W. J. Briels, J. Chem. Phys. **119**, 2363 (2003).
[68] R. Goetz, G. Gompper, and R. Lipowsky, Phys. Rev. Lett. **82**, 221 (1999).
[69] G. Illya, R. Lipowsky, and J. C. Shillcock, J. Chem. Phys. **122**, 244901 (2005).
[70] A. Malevanets and R. Kapral, J. Chem. Phys. **110**, 8605 (1999).
[71] O. Lenz and F. Schmid, J. Mol. Liq. **117**, 147 (2005).